High-Throughput Synthesis of Single-Layer MoS_2 Nanosheets as a Near-Infrared Photothermal-Triggered Drug Delivery for Effective Cancer Therapy

Wenyan Yin,[†,¶,*] Liang Yan,[†,¶] Jie Yu,[†,⊥] Gan Tian,[†,§] Liangjun Zhou,[†,‖] Xiaopeng Zheng,[†,‖] Xiao Zhang,[†] Yuan Yong,[†] Juan Li,[†] Zhanjun Gu,[†,*] and Yuliang Zhao[†,‡,*]

[†]CAS Key Laboratory for Biomedical Effects of Nanomaterials and Nanosafety, Institute of High Energy Physics, Chinese Academy of Sciences, Beijing 100049, China, [‡]National Center for Nanosciences and Technology of China, Beijing 100190, China, [§]College of Chemistry, Sichuan University, Chengdu 610064, China, [‖]College of Materials Science and Optoelectronic Technology, Graduate University of Chinese Academy of Sciences, Beijing 100049, China, and [⊥]Key Laboratory of Space Applied Physics and Chemistry, Ministry of Education and Key Laboratory of Polymer Science and Technology, Shaanxi province, School of Science, Northwestern Polytechnical University, Xi'an 710129, China. [¶]These authors contributed equally.

ABSTRACT We report here a simple, high-yield yet low-cost approach to design single-layer MoS_2 nanosheets with controllable size *via* an improved oleum treatment exfoliation process. By decorating MoS_2 nanosheets with chitosan, these functionalized MoS_2 nanosheets have been developed as a chemotherapeutic drug nanocarrier for near-infrared (NIR) photothermal-triggered drug delivery, facilitating the combination of chemotherapy and photothermal therapy into one system for cancer therapy. Loaded doxorubicin could be controllably released upon the photothermal effect induced by 808 nm NIR laser irradiation. *In vitro* and *in vivo* tumor ablation studies demonstrate a better synergistic therapeutic effect of the combined treatment, compared with either chemotherapy or photothermal therapy alone. Finally, MoS_2 nanosheets can also be used as a promising contrast agent in X-ray computed tomography imaging due to the obvious X-ray absorption ability of Mo. As a result, the high-throughput oleum treatment exfoliation process could be extended for fabricating other 2D nanomaterials, and the NIR-triggered drug release strategy was encouraging for simultaneous imaging-guided cancer theranostic application.

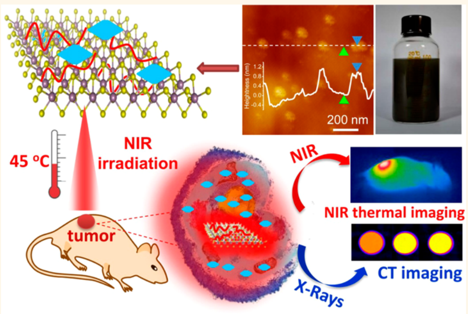

KEYWORDS: single-layer MoS_2 nanosheets · high-throughput · oleum treatment · exfoliation strategy · NIR-triggered drug delivery

Due to the multilevel complexities and variability, cancer remains one of the most challenging health problems to human beings.[1,2] To date, chemotherapy has been clinically accepted as one of the main approaches for cancer treatment.[3] However, the commonly available chemotherapeutic agents involve inevitable drawbacks of insufficient water-solubility, low cellular uptake efficiency, many side effects, and nonspecific delivery.[4] Compared with the conventional chemotherapy, a stimuli-responsive system employing "smart" nanoparticles as drug carriers has become a promising modality for improving the efficacy of the chemotherapy due to the ability of controlling drug release spatially/temporally as well as concurrently enhancing the drug uptake by cancer cells.[5−10] Recently, a near-infrared (NIR) light-induced photothermal-responsive system has gained acceptance as an elegant and efficient stimuli-responsive strategy for on-demand drug delivery in consideration of the noninvasive modality to tumor treatment and high spatial resolution of NIR laser as well as minimal damage to normal tissues.[11−13] Importantly, this system exhibits synergistic cancer therapy associated with NIR-mediated hyperthermia and heat-induced local drug release.[14−16] Thus, great effort is being devoted to fabricate a NIR photothermal-responsive drug delivery system with low cost and encouraging cancer therapy effects.

Graphene, a single atomic layer of carbon atoms packed into a two-dimensional (2D) honeycomb lattice,[17] has attracted tremendous interest in a wealth of fields, such as electrics, energy storage, catalysis, and biomedical field due to the novel physical and chemical properties.[18−21] Because of these

* Address correspondence to
zjgu@ihep.ac.cn,
zhaoyuliang@ihep.ac.cn,
yinwy@ihep.ac.cn.

Received for review March 25, 2014
and accepted June 6, 2014.

10.1021/nn501647j

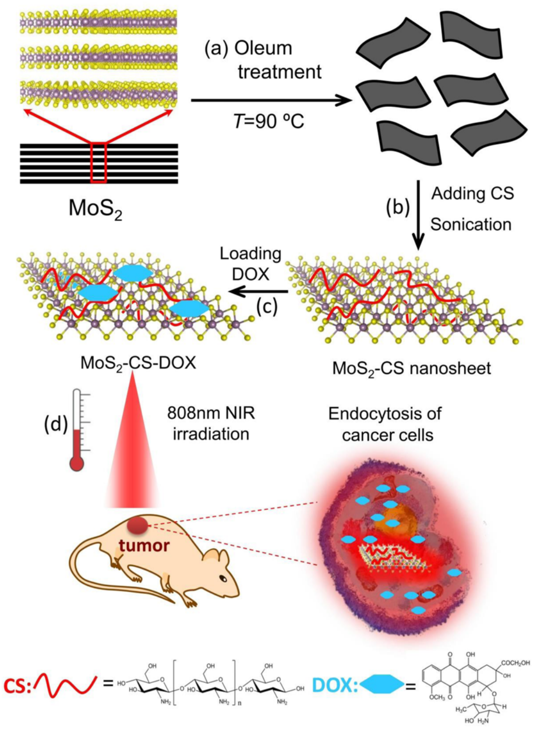

Scheme 1. Schematic illustration of the high-throughput synthesis of MoS$_2$-CS nanosheets as a NIR photothermal-triggered drug delivery system for efficient cancer therapy. (a,b) oleum treatment exfoliation process to produce single-layer MoS$_2$ nanosheets and then modified with CS, (c) DOX loading process, and (d) NIR photothermal-triggered drug delivery of the MoS$_2$ nanosheets to the tumor site.

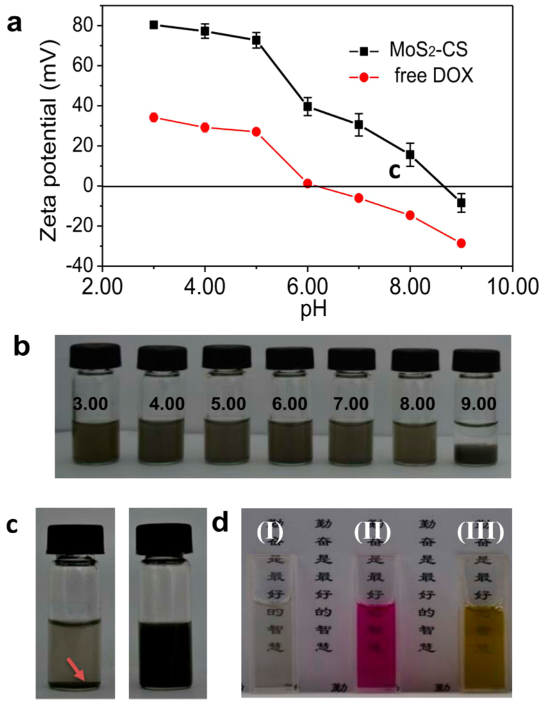

Figure 1. (a) Zeta-potential of MoS$_2$-CS and DOX in water with different pH values. (b) Digital photographs of MoS$_2$-CS aqueous dispersions in water with different pH values (concentration = 500 μg/mL). (c) Digital photographs for the dispersion status of commercial MoS$_2$ flakes (left) and MoS$_2$-CS nanosheets (right) at least 1 week. Concentration = 1 mg/mL. (d) Digital photographs of MoS$_2$-CS nanosheet dispersions with a concentration of 30 μg/mL in PBS buffer (I), cell culture medium RPMI 1640 (II), and FBS (III) at least 1 week.

outstanding properties, some effort has been devoted to explore another ultrathin 2D layered graphene analogue.[22,23] Single-layer MoS$_2$, as one of the typical layered metal dichalcogenides, has been widely studied and applied in many applications, including nanoelectronics and catalysis.[24−27] Besides, for the biomedical application, alternatively, Chou *et al.* first demonstrated the possibility of using single-layer MoS$_2$ sheets as a novel NIR absorbing agent, which showed higher absorbance in the NIR region than that of both graphene and gold nanorods.[28] Therefore, MoS$_2$ sheets would be endowed with great potential for a NIR-triggered drug delivery system in the biomedical field due to their advantages including strong NIR photothermal absorption and unique 2D structure. Unfortunately, the exploration of the single-layer MoS$_2$ sheet in the area of biomedicine is still in its infancy, mainly suffering from the complicated synthesis process, low yield of single-layer MoS$_2$, and undesired micrometer sizes.[29,30] Consequently, the development of a simple, high-throughput yet low-cost method to obtain single-layer MoS$_2$ nanosheets with controllable sizes remains a formidable challenge which imposes great limitation on the use of the MoS$_2$ nanosheets for effective biomedical application.

Here, we report a simple, high-throughput, and low-cost method for synthesis of single-layer MoS$_2$ nanosheets with controllable sizes *via* a modified oleum treatment exfoliation process (Scheme 1a). To improve the physiological stability and biocompatibility of MoS$_2$ nanosheets, chitosan (CS), a naturally occurring linear cationic polysaccharide with widespread bioapplications, is introduced during the exfoliation process (Scheme 1b). The chitosan-functionalized MoS$_2$ (MoS$_2$-CS) nanosheets can be engineered as a highly effective NIR stimuli-responsive system for simultaneous chemo-photothermal therapy, and the synergy is demonstrated by the results of the tumor ablation study (Scheme 1c,d). Remarkably, an effective healing of pancreatic cancer under a NIR-controlled drug release system is observed. In addition, we first investigate the X-ray attenuation ability of the Mo-based MoS$_2$ nanosheets and approve that these nanosheets can also serve as a promising contrast agent in X-ray computed tomography (CT) imaging. As a result, the single-layer MoS$_2$ nanosheets not only provide a novel nanoplatform for cooperative therapy system construction, resulting in a higher antitumor efficacy, but also encourage further potential investigation for imaging-guided biomedical applications.

RESULTS AND DISCUSSION

Scheme 1 demonstrates the synthesis process of single-layer MoS$_2$ nanosheets and the NIR-triggered

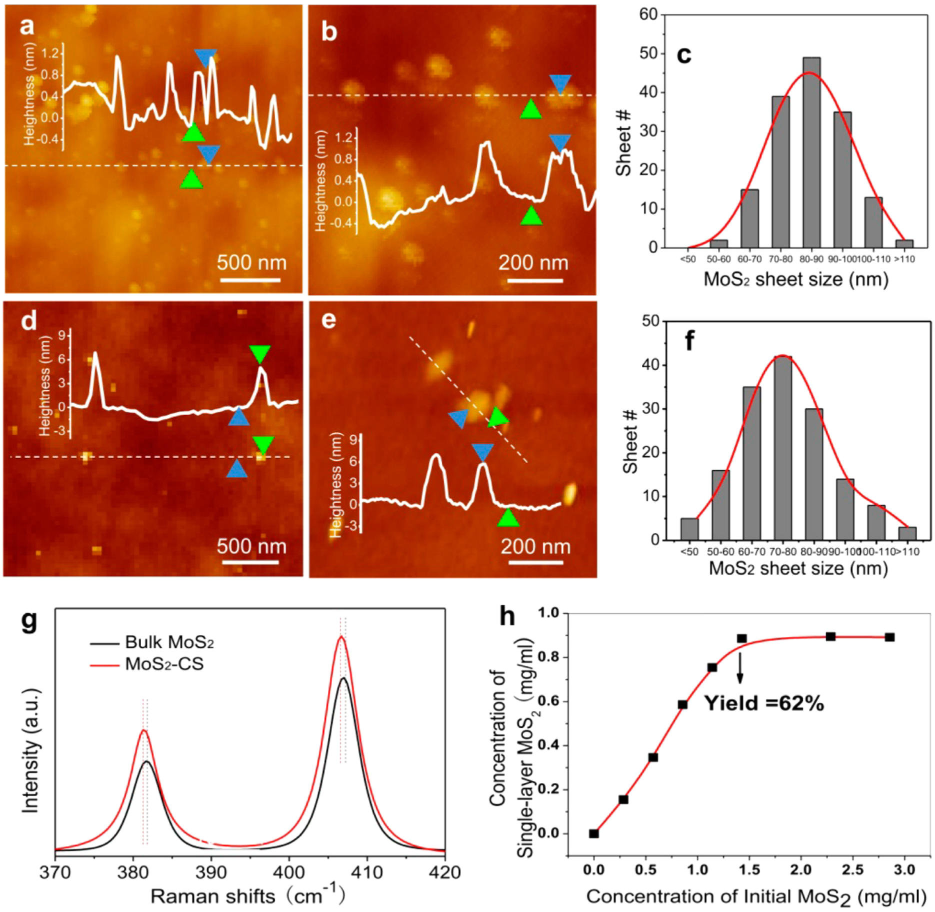

Figure 2. Characterization of MoS_2-CS nanosheets. (a,b,d,e) AFM images of a typical single-layer MoS_2 and MoS_2-CS nanosheets in sizes and with topographic heights of 0.8−1.0 and 4−6 nm, respectively. (c,f) Histograms of MoS_2 and MoS_2-CS nanosheet lateral sizes, respectively. (g) Raman spectra of commercial MoS_2 and MoS_2-CS. (h) Concentration of MoS_2-CS nanosheets after centrifugation (2000 rpm) as a function of initial MoS_2 concentration.

release of drug from the MoS_2 nanocarrier for cancer therapy. First, commercial MoS_2 flakes were ground with NaCl and treated with oleum at 90 °C under stirring. After removing oleum, we then sonicated the oleum-treated MoS_2 solution to form a grayish dispersion. Low-speed centrifugation was then applied to remove the unexfoliated MoS_2 flakes. Moreover, CS was introduced alternatively to functionalize MoS_2 nanosheets before sonication treatment. Finally, a homogeneous and water-soluble black dispersion of MoS_2-CS was obtained. The surface charge (zeta-potential) of the MoS_2-CS nanosheets indicates that they are highly positively charged when dispersed in water with various pH values, which can form stable MoS_2-CS dispersions (Figure 1a,b). As expected, compared with the commercial MoS_2 flakes, the MoS_2-CS nanosheets exhibit a well-dispersed state in deionized water even at the concentration up to 1 mg/mL (Figure 1c). Alternatively, the MoS_2-CS nanosheets could also be easily stored in various physiological solutions for at least 1 week and showed good stability (Figure 1d).

Atomic force microscopy (AFM) images reveal that the thickness of MoS_2-CS nanosheets (Figure 2d,e) with uniform shapes increases to 4−6 nm compared to the nonfunctionalized single-layer MoS_2 nanosheets (0.8−1.0 nm) (Figure 2a−c), mainly due to the attachment of CS on both planes of MoS_2 nanosheets. The average size of MoS_2-CS is ~80 nm ($n \approx 120$ sheets) (Figure 2f), in good agreement with the observation of transmission electron microscopy (TEM) measurement (Supporting Information Figure S1). Furthermore, single-layer MoS_2 nanosheets with an average diameter of 160 nm were also prepared with only 1 h sonication. The result suggests that the size of MoS_2 nanosheets could be tuned by changing the sonication time (Figure S2). The presence of CS is further proven by the results of Fourier transform infrared (FT-IR) spectroscopy (Figure S3) and thermal gravimetric analysis (TGA) (Figure S4). Raman spectra of MoS_2-CS nanosheets show the well-known in-plane $E_{2g}{}^1$ and out-of-plane A_{1g} peaks of layered 2H-MoS_2 (Figure 2g). However, owing to the sonication treatment and functionalization, broadening and shifting of the Raman bands are observed compared to the bulk MoS_2.[31]

A low yield of single-layer MoS_2 nanosheets is one of the problems that seriously hinders their biomedical application. Therefore, we further carried out a series of

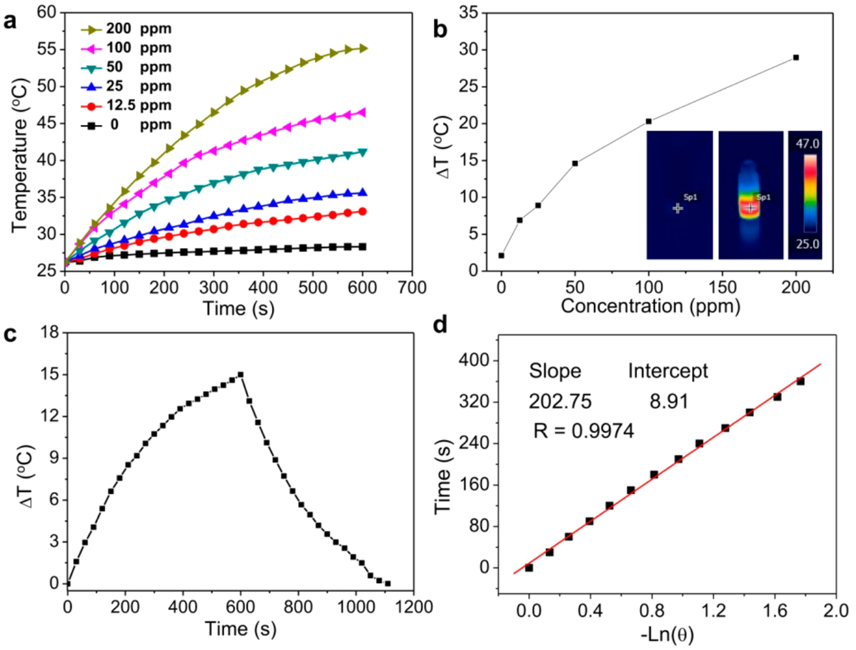

Figure 3. Photothermal profile of MoS_2-CS nanosheets. (a) Temperature increase of water and MoS_2-CS dispersions with different concentrations as a function of irradiation time. (b) Plot of temperature change over a period of 10 min *versus* MoS_2-CS concentration. Inset: Infrared thermal images of MoS_2-CS dispersion when irradiated for 0 min (left) and 10 min (right), and the joint spider stand for the irradiated spot of NIR. (c) Photothermal effect of the irradiation of MoS_2-CS dispersion with the NIR laser. The laser was shut off after irradiation for 10 min. (d) Plot of cooling period (after 600 s) *versus* negative natural logarithm of driving force temperature. Time constant (τ_s) for heat transfer from the system is determined to be 202.75 s.

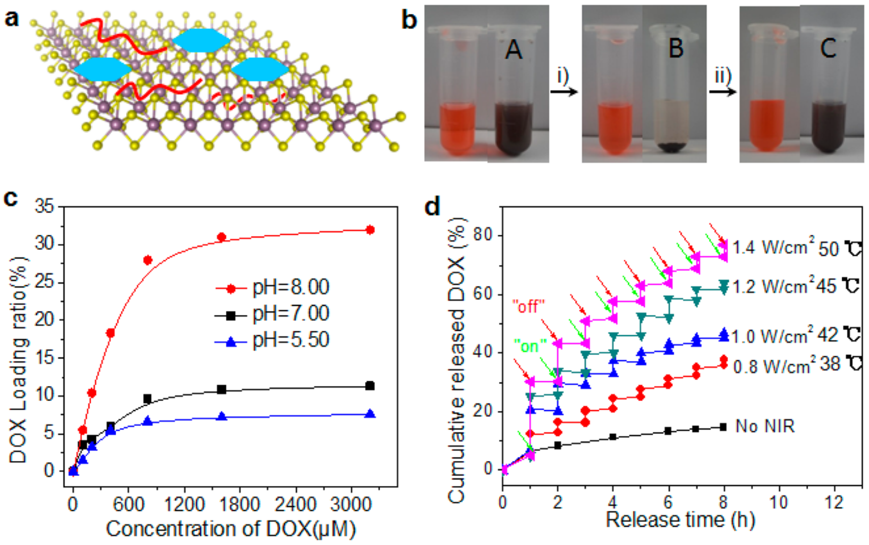

Figure 4. Drug loading and photothermal-triggered release properties of MoS_2-CS nanosheets. (a) Schematic of the loading of DOX onto the MoS_2-CS surface. (b) Photographs of a comparison of free DOX (left, orange color, 300 μM) and MoS_2-CS-DOX (DOX = 300 μM) solutions (right, black color) after centrifugation (i) and sonication (ii). (c) Plots of loading ratio of DOX onto MoS_2-CS nanosheets *versus* the concentration of DOX at different pH values. (d) Release profile of DOX in PBS buffer (pH 5.00) in the absence and presence of 808 nm NIR laser.

experiment parameters to obtain an efficient method for high-throughput synthesis of single-layer MoS_2 nanosheets. In our experiment, the presence of CS not only improves the biocompatibility and stability of MoS_2 nanosheets but also increases the stripping efficiency by preventing the rapid reaggregation driven by the large surface energy of MoS_2.[32] Based on the CS-modified MoS_2, two strategies can be used to increase the yield of MoS_2-CS nanosheets. One strategy is to increase the initial MoS_2 concentration. As shown in Figure 2h, a linear increase in the yield of single-layer MoS_2 nanosheets is obtained for the initial concentration of MoS_2 increase from 0.29 to 1.43 mg/mL. However, the yield then reaches a plateau even with the initial concentration of MoS_2 as high as 2.9 mg/mL. The maximum yield of single-layer MoS_2 nanosheets can reach up to ∼62%, which is much higher than that of the surfactant exfoliation method.[33] A large amount of (100 mL, ∼1.0 mg/mL) MoS_2-CS dispersion prepared by the method can be obtained and is well-dispersed in deionized water for long-term (Figure S5). The other strategy is to control the ultrasonic power. For example, the yield of single-layer MoS_2-CS nanosheets could increase from 62 to 70% with the probe sonication power increasing from 320 to 400 W. Compared with the traditional lithium ion intercalation method, which was conducted in high temperature using dangerous *n*-butyllithium, our method is simple, quick, safe, and the whole process can be carried out in ambient conditions.[29]

To verify the potential of using MoS_2-CS in photothermal-controlled release of antitumor drugs, NIR absorbance by MoS_2-CS was measured. It can be found that the MoS_2-CS reveals a broad NIR absorption band even at a low concentration of 25 μg/mL (Figure S6a). Then, MoS_2-CS aqueous solution with different concentrations was irradiated with an 808 nm NIR laser to investigate the photothermal heating effects. In marked contrast to the water sample, the MoS_2-CS solution shows a concentration-dependent temperature increase (Figure 3a,b). To further investigate the photothermal transduction ability of MoS_2-CS aqueous solution, we recorded the temperature change of the sample (100 μg/mL) as a function of time under the 808 nm laser (1.0 W/cm^2) for 600 s (Figure 3c,d). According to the obtained data (Figures 3c,d and S6b), the photothermal conversion efficiency of MoS_2-CS can reach ∼24.37% (Supporting Information).

Another advantage of MoS_2-CS nanosheets is their application for drug delivery due to the 2D nature. We loaded a commonly used chemotherapeutic drug, doxorubicin (DOX), on the MoS_2-CS nanosheets to obtain the MoS_2-CS-DOX (Figure 4a). DOX is noncovalently loaded onto MoS_2-CS by simple mixing under controlled pH values (5.50, 7.00, and 8.00). After removing unbound drug molecules by centrifugation, DOX loaded on the surface of MoS_2-CS is proven by the dark red color of the MoS_2-CS-DOX dispersion (Figure 4b), which is further confirmed by FT-IR (Figure S3) and UV−vis spectroscopy (Figure S6a). The close to colorless solution of B in Figure 4b after centrifugation indicated that DOX was effectively loaded onto MoS_2-CS compared with the orange color of free DOX. After sonication (C), the MoS_2-CS-DOX can be well-dispersed without obvious aggregation. Furthermore, because the fluorescence of DOX can be quenched by MoS_2-CS nanosheets (Figure S8), the UV−vis spectrograph of the liquid supernatant after centrifugation was employed to quantify the DOX attached to the MoS_2-CS from the absorbance at 480 nm. Figure 4c shows that the saturated loading efficiency gradually increases with the increase of pH values and reaches up to ∼32% at pH 8.00. The DOX release profile was examined by monitoring the increasing absorbance at 500 nm at known time intervals. As shown in Figure 4d, without laser irradiation, only ∼6% DOX is released within 60 min at room temperature. Importantly, the release of DOX is sharply increased to 12.4% when MoS_2-CS-DOX is irradiated for 10 min (0.8 W/cm^2), whereas only 0.2% of DOX is released during the subsequent 60 min of incubation without exposure to the NIR laser. Finally, the accumulated release of DOX over the whole course approaches 38%, which is much higher than that of DOX released from the control. Moreover, DOX released from MoS_2-CS-DOX is demonstrated in a power-dependent manner. About 80% of DOX is released when the power reaches 1.4 W/cm^2.

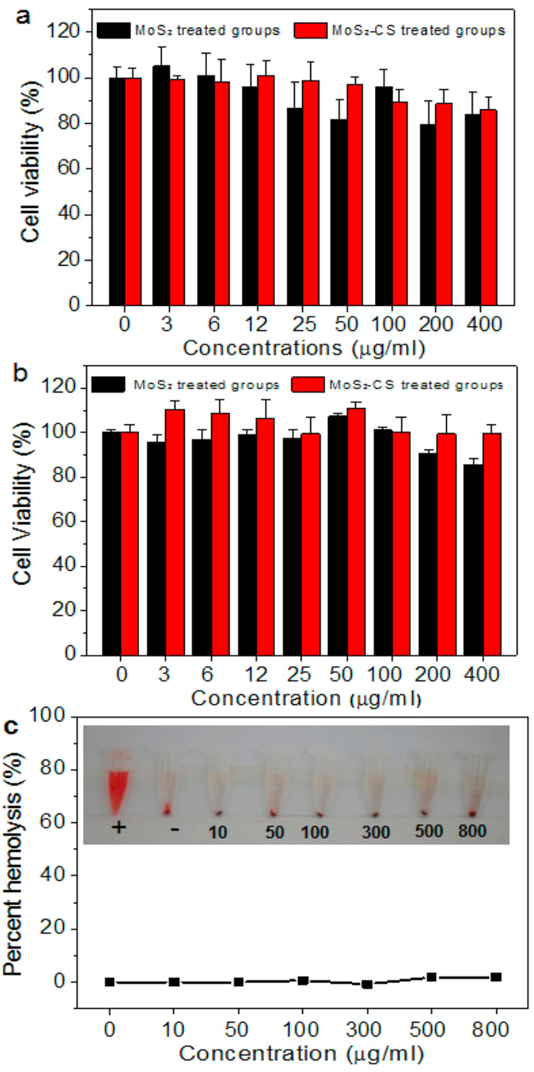

Figure 5. Viabilities of (a) KB cells and (b) Panc-1 cells incubated with MoS_2 and MoS_2-CS with different concentrations for 24 h. (c) Hemolytic percent of RBCs incubated with MoS_2-CS at various concentrations for 3 h, using deionized water (+) and PBS (−) as positive and negative controls, respectively. Inset: Photographs for direct observation of hemolysis, suggesting that MoS_2-based nanosheets exhibit good biocompatibility.

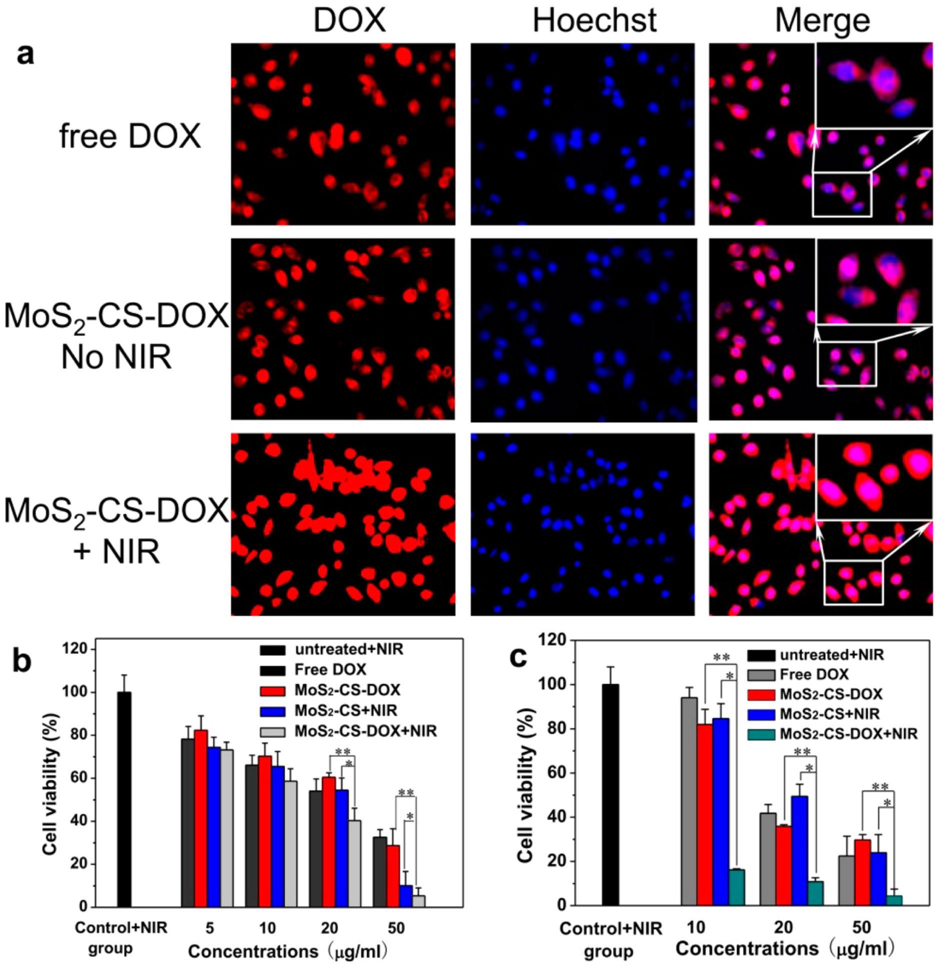

Figure 6. (a) Fluorescence images of KB cells treated with free DOX, MoS_2-CS-DOX, and MoS_2-CS-DOX under 808 nm NIR irradiation (inset: high magnification of the rectangle area). Cytotoxicity of (b) KB cells and (c) Panc-1 cells treated with MoS_2-CS with different concentrations, with or without irradiation (power = 1.0 W/cm^2). Cytotoxicity assays of (b) KB cells and (c) Panc-1 cells in the presence of saline, MoS_2-CS, DOX, MoS_2-CS upon NIR irradiation, and MoS_2-CS-DOX without or with irradiation (power = 1.0 W/cm^2).

These results distinctly indicate that the NIR-light-induced local hyperthermia can act as a stimulus for the on−off control of DOX release from MoS_2-CS-DOX. The remarkable spatial/temporal resolution profile may open up a new possibility for a better on-demand drug delivery system which can enhance antitumor efficacy.

Biocompatibility is an essential concern when it comes to the development of nanomaterials for biomedical application. Herein, viabilities of two kinds of cells, KB (human epithelial carcinoma cell line) and Panc-1 (pancreatic carcinoma, epithelial-like cell line), were measured after exposed to MoS_2 and MoS_2-CS, respectively. Figure 5a,b shows that MoS_2-CS is more biocompatible than MoS_2, demonstrating the significance of the CS functionalization process. In addition, we also investigated the influence of MoS_2-CS on hemolytic behavior of red blood cells (RBCs) to further evaluate its biocompatibility, where deionized water and phosphate buffered saline (PBS) were denoted as positive and negative controls, respectively. It is found that negligible hemolysis of RBCs is detected, indicating that MoS_2-CS possesses admirable blood compatibility (Figure 5c).Therefore, the low cytotoxicity and hemolytic activity demonstrate that MoS_2-CS exhibits good biocompatibility and thus can act as a promising nanoplatform for cancer treatment.

Having established that the drug release system is NIR-controllable, cellular uptake of DOX upon 808 nm NIR irradiation was further evaluated by fluorescence microscopy. With KB cells as an example, in a typical experiment, the MoS_2-CS-DOX samples with the same concentration were incubated with KB cells in three different culture dishes. After incubation with MoS_2-CS-DOX for 2 h, we observe that DOX fluorescence signals are distributed inside cells, indicating the efficient uptake of MoS_2-CS-DOX by cells (Figure 6a). After NIR irradiation, the red fluorescence signals inside cells become much higher, clearly suggesting that more free DOX molecules are released from the intracellular MoS_2-CS-DOX. Furthermore, the colocalization of DOX and Hoechst signals in the overlay images shows that more DOX molecules penetrate into nuclei

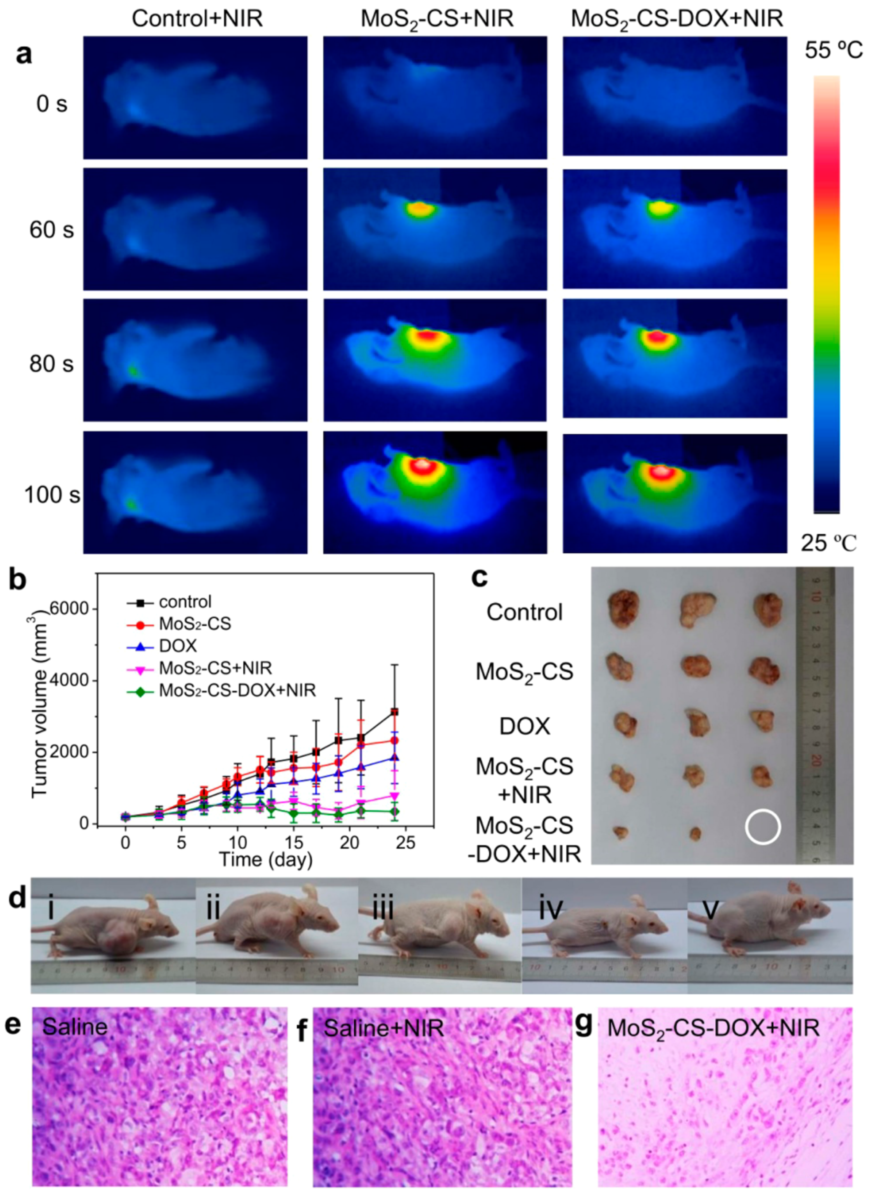

Figure 7. Comparative investigation of inhibiting tumor effectiveness *in vivo*. (a) Infrared thermal images of Panc-1 tumor-bearing mice injected with saline, MoS_2-CS+NIR, and MoS_2-CS-DOX+NIR laser. (b) Tumor growth curves of tumors after various treatments for five groups. (c) Photograph of tumors from the control group, MoS_2-CS group, DOX group, MoS_2-CS+NIR group, and MoS_2-CS-DOX+NIR group. (d) Photographs of the typical mice of tested groups corresponding to saline+NIR (i), MoS_2-CS (ii), DOX (iii), MoS_2-CS+NIR (iv), and MoS_2-CS-DOX (v) after observation for 24 days. (e−g) Histological images of tumors collected from the groups of saline (e), saline+NIR (f), and MoS_2-CS-DOX+NIR (g).

after NIR irradiation. In contrast, less DOX molecules accumulate inside nuclei in both the free DOX group and MoS_2-CS-DOX group without NIR laser. As a result, MoS_2-CS plays a significant role in regulating the release of DOX molecules and then enhancing their nuclear accumulation under NIR irradiation. To further demonstrate the therapeutic efficacy of the NIR photothermal-responsive drug delivery system, the relative cell viabilities of KB and Panc-1 cells treated with MoS_2-CS, free DOX, and MoS_2-CS-DOX with or without NIR irradiation were determined (Figure 6b,c). After being incubated with various treatments, there is a significant difference of the cell-killing effect between MoS_2-CS-DOX+NIR laser and MoS_2-CS-DOX alone. Herein, the MoS_2-CS+DOX and MoS_2-CS-DOX+NIR groups have an equivalent DOX dosage to that of the free DOX group. For the KB cells, MoS_2-CS-DOX+NIR shows higher potency against KB cells at all the tested concentrations than the chemotherapy and photothermal therapy alone (Figure 6b). For example, when KB cells were incubated with MoS_2-CS-DOX+NIR (DOX concentration = 50 μg/mL, 1.0 W/cm^2), the cell viability is remarkably reduced to 5%, which is evidently lower than that of the MoS_2-CS-DOX alone and the MoS_2-CS+NIR. For the Panc-1 cells, neither the MoS_2-CS-DOX nor MoS_2-CS+NIR shows obvious cytotoxicity with

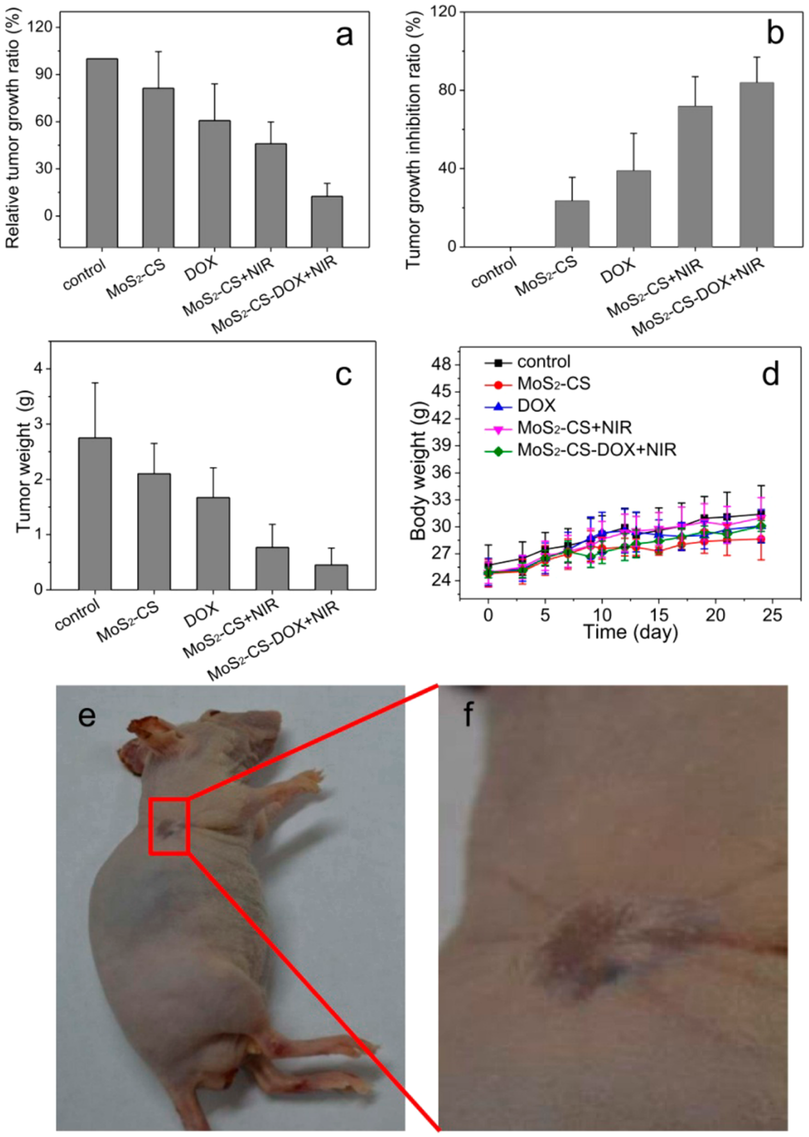

Figure 8. **Relative tumor growth ratio (a), tumor growth inhibition ratio (b), tumor weight (c), and body weight (d) of mice from the control group, MoS_2-CS group, DOX group, MoS_2-CS+NIR group, and MoS_2-CS-DOX+NIR group, respectively. (e,f) Photographs of the test mouse on the 24th day. This result showed that the tumor treated with MoS_2-CS-DOX under 808 nm NIR irradiation regressed completely, became scar tissue after 10 days, and finally vanished. Moreover, no tumor regrowth was observed again in this treated group until the study finished.**

a concentration up to 50 μg/mL, while MoS_2-CS-DOX+NIR displays remarkable cell-killing ability at each concentration, confirming the superior therapeutic efficacy in synergistic fashion of hyperthermia and chemotherapy (Figure 6c). As a result, MoS_2-CS-DOX exhibits photothermally enhanced antitumor activities when irradiated with an 808 nm NIR laser. The greatly improved therapeutic effect may be attributed to the combination of hyperthermia of MoS_2-CS with chemotherapy, which can effectively enhance the sensitivity of the delivery and release of DOX into cells and then enhance cell-killing ability, corresponding to the result in Figure 6a.

To shed more light on the therapeutic effects of MoS_2-CS nanocarriers on cancer cells, comparative studies of inhibiting tumor effectiveness *in vivo* was further investigated. Since pancreatic cancer remains one of the most difficult-to-treat cancers with a 5 year survival rate of less than 6%,[34] the Panc-1 cell was selected to evaluate the effect of the treatment. Five groups of Panc-1 tumor-bearing nude mice were set up as follows: control group, MoS_2-CS group, DOX group, MoS_2-CS+NIR group, and MoS_2-CS-DOX+NIR group. After samples were injected *via* intratumoral injection, infrared thermal images were recorded at different time points under 808 nm NIR irradiation (0.9 W/cm^2) (Figure S9). This indicated that the temperature of the tumors on the MoS_2-CS-DOX injected mice quickly increased and could readily reach a level (ΔT = 22.5 °C) which could induce hyperthermia and heat-induced drug release to kill the tumor (Figure 7a and Figure S10). However, the tumor temperature of

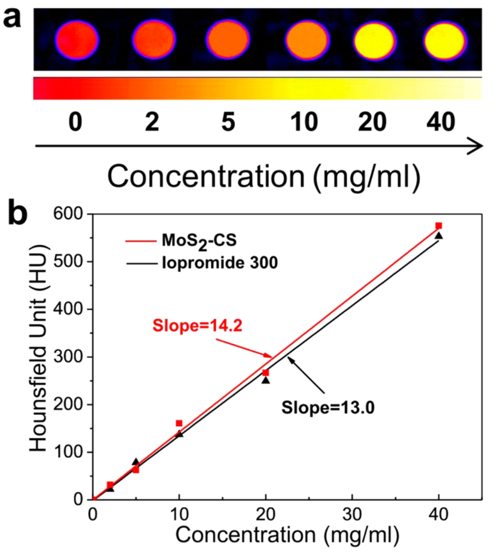

Figure 9. (a) CT image of the aqueous suspension MoS_2-CS at varied concentrations and (b) the HU values of MoS_2-CS and Iopromide 300 aqueous solution. Deionized water with 0.5% agarose was the reference.

the control group treated with saline shows insignificant change ($\Delta T = 3$ °C). The tumor volumes of each group were measured and were then plotted as a function of time (Figure 7b). Compared with the control group, efficient inhibition of tumor growth is observed for the group treated with MoS_2-CS under NIR laser irradiation (Figure 8a,b). Especially, the mean tumor volume in the MoS_2-CS-DOX+NIR group is the smallest among all treated groups, which demonstrates that MoS_2-CS-DOX can effectively inhibit tumor growth under the NIR laser irradiation.

After 24 days, all the mice were sacrificed, and then tumors were excised and weighed. The tumor photographs and mean tumor weights in each group are shown in Figure 7c and Figure 8c, respectively. The mean tumor weight in the MoS_2-CS-DOX+NIR group is the lightest among all the groups, further indicating that MoS_2-CS-DOX can more effectively inhibit tumor growth under 808 nm NIR irradiation. The reason could be attributed to (i) the combination of photothermal with chemotherapy therapy, both of which were activated simultaneously by 808 nm laser, and (ii) enhanced on-demand release of DOX from MoS_2-CS-DOX after laser irradiation, ultimately inhibiting tumor growth. Moreover, due to high toxicity always leading to a significant weight loss, the body weight of these mice were measured during the treatments, and no obvious weight loss was observed (Figure 8d), indicating the low toxicity of the treatments *in vivo*. Significantly, one of the tumors on the three mice handled with MoS_2-CS-DOX+NIR presented a black scar after 3 days, then diminished gradually, and finally fell off after another 10 days (Figure 7d and Figure 8e,f). This result indicates that the NIR photothermal effect enhancing drug delivery can even cause tumor destruction without recurrence. Histological examinations of tumors further clarify the evolution of the MoS_2-CS-DOX-treated cancer cells with increasing temperature (Figure 7e−f and Figure S11). Compared with the control groups (Figure 7e,f), when $\Delta T = 14$ °C (laser power = 0.5 W/cm^2), part of tumor tissue exhibits significant swelling, and others show organized vacuolar degeneration, which mainly was caused by photothermal ablation. However, there is no obvious signal of necrosis in Figure S11a. After ΔT reaches 17 °C (laser power = 0.7 W/cm^2), most of DOX releases from MoS_2-CS-DOX, and thus the structure of tumor tissue begins vacuolar degeneration and part of the signal of necrosis is observed (Figure S11b). However, when $\Delta T = 22.5$ °C in Figure 7g (laser power = 0.9 W/cm^2), most of tumor tissues die from necrosis, including eosinophilic cytoplasm, abundant karyorrhectic debris, and nuclear damage compared with the control group and control+NIR group. These results demonstrate that, at low temperature, photothermal ablation plays a significant role in inhibiting tumor growth; however, at high temperature, the synergistic effect of photothermal and chemotherapy is activated and devoted to killing cancer cells. Taken together with the good biocompatibility *in vivo* of this treatment (Figure 8d), MoS_2-based nanosheets have great potential as an ideal nanoplatform for simultaneous control of drug release and induction of photothermal ablation of cancer cells *in vivo via* NIR irradiation.[34]

Besides the versatile NIR photothermal-triggered drug release of MoS_2-based nanosheets for tumor treatment application, we then investigated whether these Mo-based MoS_2-CS nanosheets could act as a contrast agent for CT imaging, a widely used imaging technique in diagnostic medicine due to advantages such as deep tissue penetration and high resolution,[35] since many reports have demonstrated that nanomaterials containing high atomic number elements such as Yb, Bi, and Ta have excellent X-ray attenuation ability.[36,37] Figure 9a showed the X-ray CT image of Mo-containing MoS_2-CS nanosheets, exhibiting obvious signal enhancement with the concentration increase of the agents. To further confirm the efficiency of the MoS_2-CS nanosheets, the CT values, called Hounsfield Units (HU), were investigated. As shown in Figure 9b, the slope of the CT value for MoS_2-CS was about 14.2, which was slightly higher than that of the commercially used Iopromide 300 contrast agent, indicating that the MoS_2-CS nanosheets have the potential as a new CT contrast agent.

CONCLUSION

In summary, MoS_2-CS nanosheets with controllable sizes were prepared from commercial MoS_2 flakes *via* a safe, yet simple oleum treatment exfoliation method. The maximum yield of single-layer MoS_2-CS nanosheets can reach to ~62−70%, which is much higher than that of the surfactant exfoliation method. The as-made MoS_2-CS nanosheets are well-dispersed in water and other physiological buffers, exhibiting high stability and biocompatibility. The MoS_2-CS nanosheets have high absorption in the NIR region and can effectively convert absorbed NIR light to heat with photothermal conversion efficiency of 24.37%. After being loaded with DOX molecules, controllable drug release responsive to 808 nm NIR laser is demonstrated. Furthermore, the MoS_2-CS-based drug delivery system can be used for synergistic cancer therapy associated with NIR-mediated hyperthermia and heat-induced local drug release *in vitro* and *in vivo*. An effective treatment of pancreatic cancer *in vivo* under NIR irradiation is obtained, indicating that synergistic efficacy of hyperthermia and chemotherapy is better than hyperthermia or chemotherapy alone. Additionally, we first find that the Mo-based MoS_2 nanosheets can be used as a contrast agent in CT imaging. Therefore, we anticipate that the 2D MoS_2-based on-demand drug delivery system will turn out to be a promising cancer therapy agent, which will implicate increased opportunities for simultaneous imaging diagnosis and efficient therapy in the biomedical field.

EXPERIMENTAL SECTION

Materials. Molybdenum(IV) sulfide (MoS_2, 99%) was purchased from Alfa Aesar. Chitosan was purchased from J&K Chemical Ltd. Doxorubicin (DOX, 99%) was provided by Beijing Huafeng United Technology Co., Ltd. Other reagents were obtained from Beijing Chemical Reagent Co. All the chemicals were used as received without further purification. Deionized water was obtained by an 18 MΩ (SHRO-plus DI) system. CS stock solution (0.05 wt %) was prepared by dissolving CS in glacial acetic acid.

Preparation of Chitosan-Functionalized Single-Layer MoS_2 Nanosheets. Chitosan-functionalized MoS_2 nanosheets (denoted as MoS_2-CS) were prepared from commercial MoS_2 flakes *via* a safe yet simple liquid-phase exfoliation method. In brief, commercial MoS_2 flakes (~20 mg) were ground with NaCl for 60 min. Ground MoS_2 flakes were separated and collected by dissolving NaCl with deionized water and then centrifugation. After being dried at 60 °C for 24 h, the ground MoS_2 flakes were immersed into 20 mL of oleum. Then the mixture was heated to 90 °C for 8 h under a water bath. After free acid was completely removed by centrifugation and repeated washing, the oleum-treated MoS_2 flakes were dispersed into 20 mL of deionized water, and 10 mL of chitosan solution (0.05 wt %) was then added dropwise to the obtained dispersion under bath sonication treatment. After bath sonication for another 40 min, the mixture was further probe-sonicated at the power of 320 W for 2 h. MoS_2-CS thus obtained was collected by centrifuging and washed thoroughly several times with deionized water.

Characterization. The topologies of single-layer or functionalized MoS_2 nanosheets were examined by atomic force microscopy (AFM, Agilent 5500, Agilent, USA) under ambient conditions. The morphologies of the samples were further obtained by field-emission scanning electron microscopy (FE-SEM, S-4800, Hitachi High Technologies, Japan) and transmission electron microscopy (TEM, Tecnai G^2 20 S-TWIN operated at 200 kV). The micro-Raman spectroscopy (RenishawinVia Raman spectroscope) experiments were carried out under ambient conditions with 514 nm excitation from an argon ion laser. Fourier transform infrared spectra were obtained from a micro-Fourier transform infrared spectrophotometer (iN10-IZ10, Thermal Fisher). Ultraviolet−visible (UV−vis) spectrophotometer (Hitachi U-3900 spectrophotometer) was used for UV−vis absorbance measurements. Zeta-potential analyses were performed using zeta-potential analyzer (Nicomp380 ZLS plus ZETADi, PSS, USA), and all data were averaged over three measurements. To measure the photothermal heating effects of MoS_2-CS, an 808 nm NIR laser was oriented perpendicular to a quartz cuvette containing aqueous dispersions (1 mL) of MoS_2-CS nanosheets with various concentrations. An infrared thermal imager (E40, FLIR) was then used to simultaneously obtain the infrared thermal images of dispersions and record their temperature one time per 20 s.

Drug Loading. Briefly, MoS_2-CS was dispersed into phosphate buffered saline and then mixed with free DOX with different concentrations under different pH values (pH 5.50, 7.00, and 8.00). Then, the mixtures were stirred at room temperature for 24 h. Unbound excess DOX was then removed by centrifugation and repeatedly washed with PBS. The resulting MoS_2-CS-DOX was redispersed and stored at 4 °C. All supernatants were collected, and the amount of free DOX was determined by the absorbance peak of DOX at 480 nm. DOX loading efficiency was calculated with the following equation:

$$\text{loading efficiency}\,(\%) = \frac{1000MV(C_0 - C_e)}{m} \times 100\% \qquad (1)$$

where V (L) is the volume of supernatant, C_0 (mol/L) and C_e (mol/L) are the initial and equilibrium concentrations of DOX in PBS buffer, respectively, M (g/mol) is the molar mass of DOX, and m (g) is the mass of MoS_2-CS.

Photothermal-Triggered Release of DOX from MoS_2-CS-DOX. The release studies were performed at room temperature. In a typical measurement, a solution of MoS_2-CS-DOX (10 mg) in PBS (pH 5.00) was placed in a bottle and repeatedly irradiated with an 808 nm NIR laser at a power density of 1 W/cm^2 over a period of 10 min, followed by 1 h intervals with the laser turned off. At certain time intervals, 3 mL of treated dispersion was taken out and centrifuged at 12 000 rpm for 10 min. The released DOX was then quantified by UV−vis spectra. Finally, the measured dispersion as well as the precipitation was returned to the original dispersion.

***In Vitro* Cytotoxicity of MoS_2-CS Nanosheets toward Cancer Cells.** The *in vitro* cytotoxicity was measured using the Cell Counting Kit-8 (CCK-8) assay in KB and Panc-1 cells. First, KB and Panc-1 cells were seeded into a 96-well cell culture plates at the densities of 2×10^3 and 3×10^3 cells/well, respectively, in RPMI 1640 containing 10% FBS at 37 °C in a humid atmosphere of 95% air and 5% CO_2 for 24 h. Afterward, the MoS_2 and MoS_2-CS dispersions were diluted with medium to the desired concentrations and then added to each well to replace the original culture medium. After another 24 h, the culture medium was removed and replaced by 10 μL CCK-8 reagent in serum-free media. When incubated for 1 h at 37 °C, the optical densities of each well were read at 450 nm on a microplate reader (SpectraMax M2MDC, USA). Six replicates were done for each treatment group.

***In Vitro* Hemolysis Assay.** To evaluate the *in vitro* biocompatibility, 1 mL of blood samples (obtained from mice), which were stabilized by ethylenediaminetetracetic acid, was added to 2 mL of PBS, and red blood cells were separated from serum by centrifugation at 2000 rpm for 10 min, washed several times with PBS, and then diluted into 10 mL of PBS. Then, 0.2 mL of diluted RBC suspension was taken out to mix with (i) 0.8 mL of PBS as a negative control, (ii) 0.8 mL of deionized water as a positive control, and (iii) 0.8 mL of MoS_2-CS dispersions at concentrations ranging from 0 to 800 μg/mL. Afterward, all the mixtures were vortexed and kept at room temperature for 4 h and centrifuged at 12 000 rpm for 5 min. The absorbance of supernatants at 541 nm was measured by UV−vis spectrography. The hemolysis percent of RBCs was calculated using the following equation:

$$\text{hemolysis percent}\,(\%) = \frac{A_{\text{sample}} - A_{\text{negative}}}{A_{\text{positive}} - A_{\text{negative}}} \times 100\% \qquad (2)$$

where A_{sample}, A_{negative}, and A_{positive} are the absorbance of samples, the negative control, and positive control, respectively.

***In Vitro* Photothermal Ablation of MoS_2-CS for Cancer Cells.** KB and Panc-1 cells were first seeded in a 96-well plate at the densities of 5×10^3 and 5×10^3 cells/well for 24 h at 37 °C, respectively. Thereafter, the culture medium was changed, and cells were incubated with a serial of MoS_2-CS diluents at concentrations of 0−100 μg/mL. After 4 h of incubation, excess unbound nanosheets were removed and fresh complete medium was added to the wells. The cells were then exposed to an 808 nm laser at different output power densities for 8 min. After irradiation treatment, cells were incubated again at 37 °C for 24 h. Finally, CCK-8 assay was used to evaluate the cell viabilities. Four replicates were done for each treatment group.

Study of *In Vitro* Anticancer Effects of MoS_2-CS-DOX. Cells were divided into five groups: group 1 with cells only; group 2 with added MoS_2-CS only; group 3 incubated with DOX; group 4 incubated with MoS_2-CS+NIR; and group 5 incubated with MoS_2-CS-DOX+NIR. After 4 h of incubation, the culture medium was removed and cells were rinsed three times with PBS. Fresh complete medium was then added to the wells. The cells of groups 4 and 5 were exposed to an 808 nm laser at a power density of 1.0 W/cm^2 for 7 min. All the cells were then incubated again at 37 °C for another 24 h. After this treatment, CCK-8 assay was tested to evaluate the cell viabilities.

***In Vivo* Infrared Thermal Imaging.** Male BALB/c nude mice (5−7 weeks old) were purchased from Cancer Institute and Hospital, Chinese Academy of Medical Sciences. All animals were handled following the protocol approved by the Institutional Animal Care and Use Committee. The nude mice were inoculated subcutaneously with Panc-1 cells (2×10^6) in the side of the backside. Tumor size was measured periodically using calipers, and the tumors were allowed to grow to 10 mm in diameter. Afterward, the tumor-bearing nude mice were anaesthetized by pentobarbital (0.3%) at a dosage of 45 mg/kg body weight and then injected with 40 μL of saline, MoS_2-CS dispersion in saline (2.0 mg/kg), and MoS_2-CS-DOX (2.0 mg/kg) in saline, respectively, *via* intratumoral injection. Afterward, mice were imaged with an 808 nm continuous-wave NIR laser (0.5, 0.7, and 0.9 W/cm^2) for 7 min. The temperature of irradiated area was recorded one time per 20 s. All the experiments were carried out at room temperature of 20 °C. After 7 min of NIR irradiation, the temperature changes of the irradiated regions reached 14, 17, and 20.5 °C for the mice irradiated with the power density of 0.5, 0.7, and 0.9 W/cm^2, respectively.

Study of *In Vivo* Anticancer Effects of MoS_2-CS-DOX. When the mean tumor reached approximately 10 mm in diameter, the mice were divided into five groups (three mice in each group), minimizing the differences of weights and tumor sizes in each group. The mice were administered with (1) saline (40 μL)+NIR, (2) MoS_2-CS (40 μL, 2.0 mg/kg), (3) DOX (40 μL, 0.95 mg/kg), (4) MoS_2-CS (40 μL, 2.0 mg/kg)+NIR, and (5) MoS_2-CS-DOX+NIR (in terms of DOX, ~0.95 mg/kg; and in terms of MoS_2-CS, 2.0 mg/kg) through intratumoral injection. After 5 min, the tumor regions of groups 4 and 5 were irradiated with an 808 nm laser (0.9 W/cm^2, 7 min). The tumor sizes were measured by a caliper and calculated as follows:

$$V = \frac{ab^2}{2} \tag{3}$$

where V (mm^3) is the volume of the tumor and a (mm) and b (mm) are the tumor length and tumor width, respectively. The experiments were finished, and after 24 days, the mice were sacrificed and the tumors were collected and weighed.

Relative tumor growth ratio (G) was calculated as follows:

$$G\,(\%) = \frac{V_0 - V}{V_0} \times 100\% \tag{4}$$

where V_0 and V are the tumor volume of the control group and experiment group, respectively.

Tumor growth inhibition rate (IR) was calculated with the following equation:

$$\text{IR}\,(\%) = \frac{G}{G_0} \times 100\% \tag{5}$$

where G and G_0 are the relative tumor growth ratio of the control group and experiment group, respectively.

Hematoxylin and Eosin (H&E) Staining Analysis. To characterize the evolution process of the MoS_2-CS-DOX-treated tumors with increasing temperature and the synergistic effect of hyperthermia and chemotherapy under different power 808 nm irradiation, the tumor-bearing mice were divided into five groups: (1) saline, (2) saline+NIR, (3) MoS_2-CS-DOX+NIR (0.5 W/cm^2), (4) MoS_2-CS-DOX+NIR (0.7 W/cm^2), and (5) MoS_2-CS-DOX+NIR (0.9 W/cm^2). After the experiments were finished, the mice were sacrificed, and the tumors were removed, embedded in paraffin, and cryosectioned into 4 μm slices. Furthermore, the frozen slides of tumors were stained with H&E. The slices were examined under an inverted fluorescence microscope (Nikon E200), and images were captured with a digital camera (Canon450D).

CT Signal Measurement. To assess CT contrast efficiency, the commercial contrast agent, Iopromide 300, was set as the reference agent. The Iopromide 300 (commercially clinical CT agent) and MoS_2-CS nanosheets were dispersed in water containing 0.5% agarose with different concentrations over the range from 0, 2, 5, 10, 20, to 40 mg/mL. After careful preparation, the Eppendorf tubes were scanned in a XM-Tracer-130 CT imaging system (Institute of High Energy Physics, CAS), with the following parameters: tube voltage 70 kV, tube current 100 μA. The X-ray attenuation values of the samples were calculated in Hounsfield Units by averaging over the 3D-based region of interest.

Conflict of Interest: The authors declare no competing financial interest.

Acknowledgment. This work was supported by National Basic Research Programs of China (973 programs, No. 2012CB932504) and National Natural Science Foundation of China (Nos. 21001108, 21177128, 21101158).

Supporting Information Available: Additional experimental data as described in text. This material is available free of charge *via* the Internet at http://pubs.acs.org.

REFERENCES AND NOTES

1. Siegel, R.; Desantis, C.; Virgo, K.; Stein, K.; Mariotto, A.; Smith, T.; Cooper, D.; Gansler, T.; Lerro, C.; Fedewa, S.; *et al.* Cancer Treatment and Survivorship Statistics, 2012. *Ca-Cancer J. Clin.* **2012**, *62*, 220–241.
2. Siegel, R.; Naishadham, D.; Jemal, A. Cancer Statistics, 2012. *Ca-Cancer J. Clin.* **2012**, *62*, 10–29.
3. Jing, Y. K.; Wang, L.; Xia, L. J.; Chen, G. G.; Chen, Z.; Miller, W. H.; Waxman, S. Combined Effect of All-trans Retinoic Acid and Arsenic Trioxide in Acute Promyelocytic Leukemia Cells *in Vitro* and *in Vivo*. *Blood* **2001**, *97*, 264–269.
4. Kouranos, V.; Dimopoulos, G.; Vassias, A.; Syrigos, K. N. Chemotherapy-Induced Neutropenia in Lung Cancer Patients: The Role of Antibiotic Prophylaxis. *Cancer Lett.* **2011**, *313*, 9–14.
5. Kintzel, P. E.; Dorr, R. T. Anticancer Drug Renal Toxicity and Elimination: Dosing Guidelines for Altered Renal Function. *Cancer Treat. Rev.* **1995**, *21*, 33–64.
6. Davis, M. E.; Chen, Z.; Shin, D. M. Nanoparticle Therapeutics: An Emerging Treatment Modality for Cancer. *Nat. Rev. Drug Discovery* **2008**, *7*, 771–782.
7. You, J.; Shao, R.; Wei, X.; Gupta, S.; Li, C. Near-Infrared Light Triggers Release of Paclitaxel from Biodegradable Microspheres: Photothermal Effect and Enhanced Antitumor Activity. *Small* **2010**, *6*, 1022–1031.
8. Park, J. H.; Maltzahn, G.; Luvena, L. O.; Centron, A.; Hatton, T. A.; Ruoslahti, E.; Bhatia, S. N.; Sailor, M. J. Cooperative Nanoparticles for Tumor Detection and Photothermally Triggered Drug Delivery. *Adv. Mater.* **2010**, *22*, 880–885.
9. Huschka, R.; Neumann, O.; Barhoumi, A.; Halas, N. J. Visualizing Light-Triggered Release of Molecules Inside Living Cells. *Nano Lett.* **2010**, *10*, 4117–4122.
10. Bedard, M. F.; Braun, D.; Sukhorukov, G. B.; Skirtach, A. G. Toward Self-Assembly of Nanoparticles on Polymeric

Microshells: Near-IR Release and Permeability. *ACS Nano* **2008**, *2*, 1807–1816.

11. Welsher, K.; Liu, Z.; Sherlock, S. P.; Robinson, J. T.; Chen, Z.; Daranciang, D.; Dai, H. A Route to Brightly Fluorescent Carbon Nanotubes for Near-Infrared Imaging in Mice. *Nat. Nanotechnol.* **2009**, *4*, 773–780.
12. Li, Y. Y.; Liu, J. Q.; Dong, H. Q.; Liu, G. Z.; Hu, H. Q. Engineering of a Pluronic F127 Functionalized Magnetite/Graphene Nanohybrid for Chemophototherapy. *Nanotechnology* **2014**, *25*, 065602.
13. Li, N.; Zhao, P. X.; Astruc, D. Anisotropic Gold Nanoparticles: Synthesis, Properties, Applications, and Toxicity. *Angew. Chem., Int. Ed.* **2014**, *53*, 1756–1789.
14. Lee, S. M.; Kim, H. J.; Ha, Y. J.; Park, Y. N.; Lee, S. K.; Park, Y. B.; Yoo, K. H. Targeted Chemo-photothermal Treatments of Rheumatoid Arthritis Using Gold Half-Shell Multifunctional Nanoparticles. *ACS Nano* **2013**, *7*, 50–57.
15. Wang, Y.; Wang, K. Y.; Zhao, J. F.; Liu, X. G.; Bu, J.; Yan, X. Y.; Huang, R. Q. Multifunctional Mesoporous Silica-Coated Graphene Nanosheet Used for Chemo-photothermal Synergistic Targeted Therapy of Glioma. *J. Am. Chem. Soc.* **2013**, *135*, 4799–4804.
16. Dong, K.; Liu, Z.; Li, Z. H.; Ren, J. S.; Qu, X. G. Hydrophobic Anticancer Drug Delivery by a 980 nm Laser-Driven Photothermal Vehicle for Efficient Synergistic Therapy of Cancer Cells *in Vivo*. *Adv. Mater.* **2013**, *25*, 4452–4458.
17. Novoselov, K. S.; Geim, A. K.; Morozov, S. V.; Jiang, D.; Zhang, Y.; Dubonos, S. V.; Grigorieva, I. V.; Firsov, A. A. Electric Field Effect in Atomically Thin Carbon Films. *Science* **2004**, *306*, 666–669.
18. Stankovich, S.; Dikin, D. A.; Dommett, G. H. B.; Kohlhaas, K. M.; Zimney, E. J.; Stach, E. A.; Piner, R. D.; Nguyen, S. T.; Ruoff, R. S. Graphene-Based Composite Materials. *Nature* **2006**, *442*, 282–286.
19. Yang, K.; Feng, L. Z.; Shi, X. Z.; Liu, Z. Nano-Graphene in Biomedicine: Theranostic Applications. *Chem. Soc. Rev.* **2013**, *42*, 530–547.
20. Zhu, Y.; Murali, S.; Cai, W.; Li, X.; Suk, J. W.; Potts, J. R.; Rodney, S. R. Graphene and Graphene Oxide: Synthesis, Properties, and Applications. *Adv. Mater.* **2010**, *22*, 3906–3924.
21. Korkut, S.; Roy-Mayhew, J. D.; Dabbs, D. M.; Milius, D. L.; Aksay, I. A. High Surface Area Tapes Produced with Functionalized Graphene. *ACS Nano* **2011**, *5*, 5214–5222.
22. Xu, M. S.; Liang, T.; Shi, M. M.; Chen, H. Z. Graphene-like Two-Dimensional Materials. *Chem. Rev.* **2013**, *113*, 3766–3798.
23. Nicolosi, V.; Chhowalla, M.; Kanatzidis, M. G.; Strano, M. S.; Coleman, J. N. Liquid Exfoliation of Layered Materials. *Science* **2013**, *340*, 6139.
24. Radisavljevic, B.; Radenovic, A.; Brivio, J.; Giacometti, V.; Kis, A. Single-Layer MoS$_2$ Transistors. *Nat. Nanotechnol.* **2011**, *6*, 147–150.
25. Shi, Y. M.; Zhou, W.; Lu, A. Y.; Fang, W. J.; Lee, Y. H.; Hsu, A. L.; Kim, S.; Kim, K. K.; Yang, H. Y.; Li, L. J.; *et al.* van der Waals Epitaxy of MoS$_2$ Layers Using Graphene as Growth Templates. *Nano Lett.* **2012**, *12*, 2784–2791.
26. Zeng, Z. Y.; Yin, Z. Y.; Huang, X.; Li, H.; He, Q. Y.; Lu, G.; Boey, F.; Zhang, H. Single-Layer Semiconducting Nanosheets: High-Yield Preparation and Device Fabrication. *Angew. Chem., Int. Ed.* **2011**, *50*, 11093–11097.
27. Yang, L. C.; Wang, S. N.; Mao, J. J.; Deng, J. W.; Gao, Q. S.; Tang, Y.; Schmidt, O. G. Hierarchical MoS$_2$/Polyaniline Nanowires with Excellent Electrochemical Performance for Lithium-Ion Batteries. *Adv. Mater.* **2013**, *25*, 1180–1184.
28. Chou, S. S.; Kaehr, B.; Kim, J.; Foley, B. M.; De, M.; Hopkins, P. E.; Huang, J. X.; Brinker, C. J.; Dravid, V. P. Chemically Exfoliated MoS$_2$ as Near-Infrared Photothermal Agents. *Angew. Chem., Int. Ed.* **2013**, *52*, 4160–4164.
29. Zhu, C. F.; Zeng, Z. Y.; Li, H.; Li, F.; Fan, C. H.; Zhang, H. Single-Layer MoS$_2$ Based Nanoprobes for Homogeneous Detection of Biomolecules. *J. Am. Chem. Soc.* **2013**, *135*, 5998–6001.
30. Wang, Q. H.; Kalantar-Zadeh, K.; Kis, A.; Coleman, J. N.; Strano, M. S. Electronics and Optoelectronics of Two-Dimensional Transition Metal Dichalcogenides. *Nat. Nanotechnol.* **2012**, *7*, 699–712.
31. Eda, G.; Yamaguchi, H.; Voiry, D.; Fujita, T.; Chen, M.; Chhowalla, M. Photoluminescence from Chemically Exfoliated MoS$_2$. *Nano Lett.* **2011**, *11*, 5111–5116.
32. Joensen, P.; Frindt, R. F.; Morrison, S. R. Single-Layer MoS$_2$. *Mater. Res. Bull.* **1986**, *21*, 457–461.
33. Smith, R. J.; King, P. J.; Lotya, M.; Wirtz, C.; Khan, U.; De, S.; O'Neill, A.; Duesberg, G. S.; Grunlan, J. C.; Moriarty, G.; Chen, J.; *et al.* Large-Scale Exfoliation of Inorganic Layered Compounds in Aqueous Surfactant Solutions. *Adv. Mater.* **2011**, *23*, 3944–3948.
34. Wei, D.; Parsels, L. A.; Karnak, D.; Davis, M. A.; Parsels, J. D.; Marsh, A. C.; Zhao, L.; Maybaum, J.; Lawrence, T. S.; Sun, Y.; *et al.* Inhibition of Protein Phosphatase 2A Radiosensitizes Pancreatic Cancers by Modulating CDC25C/CDK1 and Homologous Recombination Repair. *Clin. Cancer Res.* **2013**, *19*, 4422–4432.
35. Shilo, M.; Reuveni, T.; Motiei, M.; Popovtzer, R. Nanoparticles as Computed Tomography Contrast Agents: Current Status and Future Perspectives. *Nanomedicine* **2012**, *7*, 257–269.
36. Liu, Z.; Li, Z.; Liu, J.; Gu, S.; Yuan, Q.; Ren, J.; Qu, X. Long-Circulating Er^{3+}-Doped Yb$_2$O$_3$ Up-conversion Nanoparticle as an *In Vivo* X-ray CT Imaging Contrast Agent. *Biomaterials* **2012**, *33*, 6748–6757.
37. Liu, Y. L.; Ai, K. L.; Lu, L. Nanoparticulate X-ray Computed Tomography Contrast Agents: From Design Validation to *In Vivo* Applications. *Acc. Chem. Res.* **2012**, *45*, 1817–1827.